International Journal of Heat and Mass Transfer 127 (2018) 308–320

Contents lists available at ScienceDirect

International Journal of Heat and Mass Transfer

journal homepage: www.elsevier.com/locate/ijhmt

A numerical study of buoyancy-Marangoni convection of volatile binary fluids in confined geometries

Tongran Qin *, Roman O. Grigoriev

School of Physics, Georgia Institute of Technology, Atlanta, GA 30332-0430, USA

ARTICLE INFO

Article history:
Received 22 March 2018
Received in revised form 25 June 2018
Accepted 28 June 2018
Available online 29 July 2018

Keywords:
Marangoni convection
Buoyancy-Marangoni convection
Multiphase flows
Two-phase flows
Phase change
Free-surface flows
Interfacial flows
Binary fluids
Multi-component transport
Surface tension effects
Thermocapillarity
Solutocapillarity
Flow stability
Heat pipes

ABSTRACT

A horizontal temperature gradient can cause a flow in a layer of liquid with a free surface via several different mechanisms. The most universal one is due to thermocapillary stresses that arise due to the temperature dependence of surface tension. For binary liquids, the flow can also be driven by solutocapillary stresses that arise due to the dependence of surface tension on the composition of the liquid. For some binary liquids, such as water-alcohol mixtures, solutocapillary stresses are primarily due to phase change (e.g., differential evaporation or condensation of the two components), and these two mechanisms can counteract each other. A recent experimental study (Li and Yoda, 2016) has demonstrated that the flow direction can be reversed by changing the amount of air present inside the experimental apparatus. To understand how the presence of air affects the interfacial stresses, we have developed and implemented numerically a comprehensive two-sided transport model, which accounts for transport of heat, mass, and momentum in both phases and phase change across the interface and is able to reproduce the experimental results. The detailed analysis of these results shows that air tends to suppress phase change and hence solutocapillary stresses. Removing the air enhances phase change, instead suppressing the variation in the interfacial temperature and hence thermocapillary stresses.

1. Introduction

Various types of convective flows can arise in layers of binary liquid during evaporation [1–5] or condensation [6–10] driven by the gradient in either vapor concentration or temperature normal to the free surface. Perhaps the most famous example is "wine tears" that form when a mixture of water and ethanol is allowed to evaporate. This mixture is an example of a positive binary fluid [11], where the more volatile component (ethanol) has lower surface tension compared with the less volatile component (water). Preferential evaporation of ethanol from a thin layer near a side wall reduces surface tension of the mixture there and generates solutocapillary forces that drive the liquid towards, and in some instances up, the wall, which is a key physical mechanism behind the formation of wine tears [12,13]. More recently it has been discovered that thermocapillary stresses generated via evaporative cooling of the liquid surface also play a role in this phenomenon [14]. In this specific case, evaporation causes the temperature near the edge of the film to decrease, further increasing surface tension, so thermocapillary stresses *enhance* solutocapillary ones.

Under certain conditions, however, thermocapillary and solutocapillary stresses can oppose each other. This property can be usefully exploited when thermocapillarity has an adverse effect, e.g., in thermal management devices, such as heat pipes, which rely on evaporative cooling. Heat pipes are effectively sealed cavities partially filled with a volatile liquid, and it is the temperature gradient tangential to the free surface that drives the system out of equilibrium and generates the flow. For pure fluids, thermocapillary stresses drive the flow away from the hot end of the heat pipe, which can cause dry-out leading to a complete loss of evaporative cooling and a dramatic increase in the temperature of the hot end. The adverse effect of thermocapillarity can be ameliorated by using a positive binary coolant [15], where the differential evaporation of the two components causes solutocapillary stresses towards, rather than away from, the hot end. Indeed, experimental studies have shown that the direction of the flow can be reversed by using a mixture of water with ethanol [16] or methanol [17]. Beneficial effects of using a binary mixture on the performance of a heat pipe in microgravity have also been demonstrated [18].

* Corresponding author.
E-mail address: tongran@gatech.edu (T. Qin).

https://doi.org/10.1016/j.ijheatmasstransfer.2018.06.141
0017-9310/

There is a vast literature on convection in binary fluids driven by a vertical [19–22] temperature gradient, but almost all of it is devoted to nonvolatile liquids, where solutocapillary stresses arise due to the Soret effect [23] rather than differential phase change. We should also mention studies of the role of solutocapillary stresses in nucleate boiling [24], droplet evaporation [25], and thin film evaporation [26]. However, other than an earlier work [27], there are no theoretical (either numerical or analytical) studies of convection in volatile binary mixtures subjected to a horizontal temperature gradient; the single relevant numerical study [28] did not consider the effects of phase change. Consequently, there is a lack of understanding of the effects of transport (of heat or mass) in the gas phase or the effects of noncondensable gases such as air. The present study addresses this gap in our understanding by introducing a comprehensive two-sided model that provides a quantitative description of transport of heat, mass, and momentum in both the liquid and the gas phase as well as across the liquid-gas interface.

The model is described in detail in Section 2. The results of the numerical investigations of this model are presented, analyzed, and compared with experimental observations reported by Li and Yoda [17] in Section 3. Our summary and conclusions are presented in Section 4.

2. Mathematical model

2.1. Governing equations

When the liquid is a binary mixture of two volatile components (in this study we will focus on the special case of water-methanol mixtures), the gas phase above the liquid layer is generally a multicomponent mixture of the vapors of the two components of the liquid and various noncondensable gases (e.g., air) that tend to be dissolved in the liquid. Under typical experimental conditions, one tends to find a ternary mixture containing air whose concentration depends on whether the liquid has been degassed and whether the cavity (cf. Fig. 1) has been evacuated before being filled with the binary liquid. The transport model describing a layer of binary liquid in local thermodynamic equilibrium with the ternary gas mixture can be constructed as a generalization of the two-sided transport models [29–32] describing single-component liquids. Both phases (liquid and gas) will be considered incompressible

$$\nabla \cdot \mathbf{u} = 0 \tag{1}$$

with momentum transport in the bulk described by the Navier-Stokes equation in the Boussinesq approximation

$$\rho(\partial_t \mathbf{u} + \mathbf{u} \cdot \nabla \mathbf{u}) = -\nabla p + \mu \nabla^2 \mathbf{u} + \rho \mathbf{g}, \tag{2}$$

where $\mathbf{u}$ is the velocity, p is the pressure, ρ and μ are the density and dynamic viscosity of the fluid, respectively, and $\mathbf{g}$ is the gravitational acceleration. Heat transport in the bulk is described by the advection-diffusion equation

$$\partial_t T + \mathbf{u} \cdot \nabla T = \alpha \nabla^2 T, \tag{3}$$

where T is the temperature and $\alpha = k/\rho C_p$ is the thermal diffusivity of the fluid.

The density of the liquid mixture is

$$\rho_l = \rho_{l,m} + \rho_{l,w}, \tag{4}$$

where $\rho_{l,b}$ is the density of component b in the mixture. Here and below the subscript denotes the phase (l for the liquid, g for the gas), and/or the component in the mixture (m for methanol, w for water, a for air). We will use the subscript i to denote the values at the liquid-gas interface. A linear dependence of the density of each component on the temperature is assumed,

$$\rho_{l,b} = \rho^0_{l,b}[1 - \beta_{l,b}(T - T_0)], \tag{5}$$

where $\beta_{l,b} = -\rho^{-1}_{l,b}\partial\rho_{l,b}/\partial T$ at $T = T_0$ is the coefficient of thermal expansion, $\rho^0_{l,b}$ is the density of component b in the mixture at the reference temperature T_0, which is given by

$$\rho^0_{l,b} = n_l Y_b m^1_b, \tag{6}$$

where n_l is the total number density in the liquid, m^1_b is the mass of one molecule, and $Y_b = n_{l,b}/n_l$ is the concentration (molar fraction) of component b in the liquid phase.

The density and pressure of the gas mixture are

$$\begin{aligned} \rho_g &= \rho_{g,m} + \rho_{g,w} + \rho_{g,a}, \\ p_g &= p_{g,m} + p_{g,w} + p_{g,a}, \end{aligned} \tag{7}$$

where all components are assumed to be ideal,

$$\begin{aligned} \rho_{g,b} &= \frac{X_b p_g}{R_b T} = n_g X_b m^1_b, \\ p_{g,b} &= X_b p_g = n_g X_b k_B T, \end{aligned} \tag{8}$$

$X_b = n_{g,b}/n_g$ is the concentration, $R_b = R/M_b$ is the specific gas constant, $M_b = m^1_b N_A$ is the molar mass of component b, and $R = k_B N_a$ is the universal gas constant. According to the Boussinesq approximation, the spatial average of ρ_l and ρ_g is used on the left-hand-side (but not the right-hand-side) of the Navier-Stokes Eq. (2) for the liquid and the gas phase.

To avoid the assumption of dilute mixtures used in formulating the transport models for simple fluids [29,32], we will describe mass transport in both phases using molar fractions rather than mass densities. The local mass/number conservation for component b (in either the liquid or the gas phase) can be described in terms of the corresponding number density n_b

$$\partial_t n_b + \mathbf{u} \cdot \nabla n_b = -\nabla \cdot \mathbf{j}_b, \tag{9}$$

where $\mathbf{j}_b$ is the diffusive number flux of component b with respect to the bulk mixture that moves with velocity $\mathbf{u}$. The liquid phase is a binary mixture, so we can use Fick's law

$$\mathbf{j}_b = -n_l D_l \nabla Y_b, \tag{10}$$

where D_l is the conventional binary mass diffusivity of the two components. With the assumptions of incompressible flow and constant total number density n_l, the local mass/number conservation Eq. (9) can be rewritten as an advection-diffusion equation for, say, the water concentration in the liquid

$$\partial_t Y_w + \mathbf{u} \cdot \nabla Y_w = \nabla \cdot (D_l \nabla Y_w) \tag{11}$$

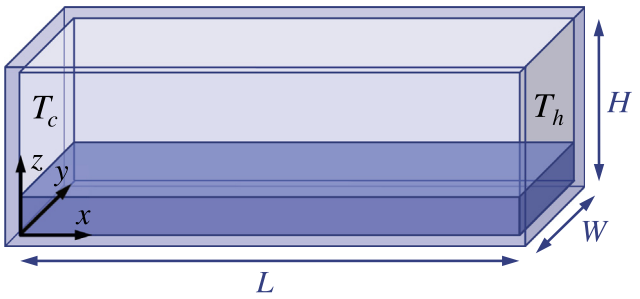

Fig. 1. A sealed test cell containing the liquid and air/vapor mixture. Gravity is pointing in the negative z direction.

with the methanol concentration recovered from

$$Y_m = 1 - Y_w. \tag{12}$$

The gas phase is a ternary mixture of methanol, water, and air. For a multi-component mixture with N components, the relation between the diffusion fluxes and the concentration gradients is given by the Maxwell-Stefan relation [33]

$$\nabla X_b = \sum_{k=1}^{N} \frac{X_b \mathbf{j}_k - X_k \mathbf{j}_b}{n_g D_{bk}}, \tag{13}$$

where $D_{bk} = D_{kb}$ is the conventional binary mass diffusivity between components b and k. The system (13) can be solved, yielding the fluxes of the first $N' = N - 1$ components

$$\begin{bmatrix} \mathbf{j}_1 \\ \vdots \\ \mathbf{j}_{N'} \end{bmatrix} = \mathbb{D} \begin{bmatrix} \nabla X_1 \\ \vdots \\ \nabla X_{N'} \end{bmatrix}, \tag{14}$$

such that the flux of the Nth component is

$$\mathbf{j}_N = -\sum_{k=1}^{N'} \mathbf{j}_k. \tag{15}$$

It should be noted that, unlike the binary mass diffusivities D_{bk}, the elements of the matrix $\mathbb{D}$ depends on the concentrations, and in general $\mathbb{D}_{bk} \neq \mathbb{D}_{kb}$.

For a ternary gas mixture considered in this study, we find

$$\begin{aligned} \mathbf{j}_m &= -n_g \mathbb{D}_{mm} \nabla X_m - n_g \mathbb{D}_{mw} \nabla X_w, \\ \mathbf{j}_w &= -n_g \mathbb{D}_{wm} \nabla X_m - n_g \mathbb{D}_{ww} \nabla X_w, \\ \mathbf{j}_a &= -\mathbf{j}_w - \mathbf{j}_m, \end{aligned} \tag{16}$$

where

$$\begin{aligned} \mathbb{D}_{mm} &= D_g^{-1}[X_m D_{ma}(D_{wa} - D_{mw}) + D_{mw} D_{ma}], \\ \mathbb{D}_{mw} &= X_m D_g^{-1} D_{wa}(D_{ma} - D_{mw}), \\ \mathbb{D}_{wm} &= X_w D_g^{-1} D_{ma}(D_{wa} - D_{mw}), \\ \mathbb{D}_{ww} &= D_g^{-1}[X_w D_{wa}(D_{ma} - D_{mw}) + D_{mw} D_{wa}], \end{aligned} \tag{17}$$

and $D_g = X_m D_{wa} + X_w D_{ma} + X_a D_{mw}$.

Note that the diffusive fluxes in a multi-component mixture generally depend on the concentration gradients of all components, so the transport Eqs. (9) are coupled. Furthermore, the dependence of the diffusion coefficients $\mathbb{D}_{bk}$ on the concentrations X_b makes these equations nonlinear. In principle, this system of equations can be solved numerically, but these two aspects make numerical solutions rather cumbersome. Different approaches have therefore been proposed [34] to decouple these differential equations. For example, after linearization about the mean concentrations, the mass diffusivity matrix $\mathbb{D}$ can be diagonalized, yielding a set of uncoupled differential equations for "pseudo-concentrations" [35–37]. The disadvantage of this approach is that the concentrations can differ substantially from the mean, with the present problem providing a good example.

A widely used alternative approach is based on the concept of effective mass diffusivity [38–42]. In particular, assuming that the off-diagonal terms in (14) are negligible, we find

$$\mathbf{j}_b = -n_g \mathfrak{D}_b \nabla X_b, \tag{18}$$

where the effective mass diffusivity $\mathfrak{D}_b$ is assumed to depend only on the composition X_b and the binary mass diffusivities D_{bk}. For the water-methanol-air mixture we are interested in, the conventional binary mass diffusivities D_{bk} between all pairs of components are of similar magnitude, and the differences between them are relatively small. Hence the off-diagonal elements of matrix $\mathbb{D}$ can indeed be neglected, such that $\mathfrak{D}_b \approx \mathbb{D}_{bb}$, and (16) reduces to

$$\begin{aligned} \mathbf{j}_m &= -n_g \mathbb{D}_{mm} \nabla X_m, \\ \mathbf{j}_w &= -n_g \mathbb{D}_{ww} \nabla X_w, \\ \mathbf{j}_a &= -\mathbf{j}_1 - \mathbf{j}_2. \end{aligned} \tag{19}$$

With the assumptions of incompressible flow and constant total number density n_g, the relation (19) allows the system (9) to be decoupled and simplified, yielding

$$\partial_t X_b + \mathbf{u} \cdot \nabla X_b = \nabla \cdot (\mathbb{D}_{bb} \nabla X_b) \tag{20}$$

for $b = m$ and w and the concentration of air given by

$$X_a = 1 - X_m - X_w. \tag{21}$$

Together, (20) and (21) describe mass transport in the ternary gas phase with arbitrary composition. Note that the number fluxes due to thermodiffusion (the Soret effect) in both phases were found to be negligible compared with those due to molecular diffusion, and hence were neglected in (10) and (19).

Finally, inside a sealed cavity, global mass conservation should be satisfied for each component

$$\begin{aligned} \int_{\text{liquid}} Y_m n_l dV + \int_{\text{gas}} X_m n_g dV &= \frac{m_m}{m_m^1}, \\ \int_{\text{liquid}} Y_w n_l dV + \int_{\text{gas}} X_w n_g dV &= \frac{m_w}{m_w^1}, \\ \int_{\text{gas}} (1 - X_m - X_w) n_g dV &= \frac{m_a}{m_a^1}, \end{aligned} \tag{22}$$

where m_b is the initial total mass of component b and

$$\begin{aligned} n_l &= \frac{\rho_{l,m}^0}{m_m^1} + \frac{\rho_{l,w}^0}{m_w^1}, \\ n_g &= \frac{p_g}{k_B T}. \end{aligned} \tag{23}$$

An external temperature gradient will cause evaporation near the hot end and condensation near the cold end, which will not necessarily balance, so the volumes of the liquid and gas phase can change. In a numerical implementation of the model, the change in the liquid volume associated with the motion of the interface would not satisfy the mass flux balance at the interface exactly, and tiny numerical errors will eventually accumulate. A small inaccuracy in evaluating the volume of the liquid phase can result in a large relative error for the mass of vapor due to the large ratio of the densities. Hence, a (spatially uniform) pressure offset p_o, methanol concentration correction ΔX_m, and water concentration correction ΔX_w are computed at each time step to enforce the three conservation laws (22) evaluated with

$$\begin{aligned} p_g &= p + p_o, \\ X_m &= X'_m + \Delta X_m, \\ X_w &= X'_w + \Delta X_w, \end{aligned} \tag{24}$$

where p is the dynamic pressure in the gas phase obtained by solving Eqs. (1) and (2), and X'_m and X'_w are the concentrations of methanol and water, respectively, obtained by solving the transport Eq. (20).

2.2. Boundary conditions

The system of coupled evolution Eqs. 1,2,3 and (11) for the liquid phase (or (20) for the gas phase) has to be solved in a

self-consistent manner, subject to the boundary conditions describing the balance of momentum, heat, and number fluxes at the liquid-gas interface and at the inner surface of the walls of the cavity. In particular, local phase equilibrium is described using Raoult's law

$$p_{g,b} = \gamma_b p_{s,b} Y_b, \tag{25}$$

where γ_b is the activity coefficient of component b, which accounts for deviations from an ideal liquid mixture, and $p_{s,b}$ is the saturation vapor pressure of pure component b, which can be related to the interfacial temperature T_i through the Antoine equation

$$\ln p_{s,b} = A_b - \frac{B_b}{C_b + T_i}, \tag{26}$$

where A_b, B_b, and C_b are empirical coefficients (see Appendix A).

Phase change occurs locally where the thermodynamic free energy is different between the phases. The driving forces for mixtures include the temperature difference, pressure difference, and concentration difference across the interface [43]. We find that the effect due to the latter two are negligible in this study. Therefore, phase change for each component of the volatile fluid can be described using the kinetic theory expression [44], which only includes the temperature difference

$$j_{b,i} = \frac{2\chi_b}{2-\chi_b} n_g X_b \sqrt{\frac{R_b T_i}{2\pi}} \frac{\mathcal{L}_b}{R_b T_i} \frac{T_i - T_{s,b}}{T_{s,b}}, \tag{27}$$

where $j_{b,i}$ is the number flux of component b across the interface, χ_b is the accommodation coefficient, $\mathcal{L}_b$ is the latent heat of phase change, and $T_{s,b}$ is the saturation temperature of component b at a given partial pressure $p_{g,b} = p_g X_b$, which can again be computed using (25) and (26).

On the gas side of the interface, with the help of (19) and taking into account the fact that air is noncondensable, we can write the mass/number flux balance as

$$\begin{aligned} j_{m,i} &= n_g X_m \hat{\mathbf{n}} \cdot (\mathbf{u}_g - \mathbf{u}_i) - n_g \mathbb{D}_{mm} \partial_n X_m, \\ j_{w,i} &= n_g X_w \hat{\mathbf{n}} \cdot (\mathbf{u}_g - \mathbf{u}_i) - n_g \mathbb{D}_{ww} \partial_n X_w, \\ j_{a,i} &= 0. \end{aligned} \tag{28}$$

Here and beyond $\hat{\mathbf{n}}$ denotes the unit vector normal to the interface. On the liquid side

$$\begin{aligned} j_{m,i} &= n_l Y_m \hat{\mathbf{n}} \cdot (\mathbf{u}_l - \mathbf{u}_i) - n_l D_l \partial_n Y_m, \\ j_{w,i} &= n_l Y_w \hat{\mathbf{n}} \cdot (\mathbf{u}_l - \mathbf{u}_i) - n_l D_l \partial_n Y_w. \end{aligned} \tag{29}$$

The heat flux balance gives

$$\mathcal{L}_m m_m^1 j_{m,i} + \mathcal{L}_w m_w^1 j_{w,i} = k_g \partial_n T_g - k_l \partial_n T_l, \tag{30}$$

where $\partial_n = \hat{\mathbf{n}} \cdot \nabla$, and the temperature is assumed continuous

$$T_l = T_g = T_i. \tag{31}$$

The tangential components of the velocity across the interface are also continuous

$$(\mathbb{I} - \hat{\mathbf{n}}\hat{\mathbf{n}}) \cdot (\mathbf{u}_l - \mathbf{u}_g) = 0, \tag{32}$$

while the normal components are related by the kinematic condition

$$n_l \hat{\mathbf{n}} \cdot (\mathbf{u}_l - \mathbf{u}_i) = n_g \hat{\mathbf{n}} \cdot (\mathbf{u}_g - \mathbf{u}_i) = j_{m,i} + j_{w,i}. \tag{33}$$

The stress balance incorporates the viscous drag between the two phases, thermocapillary and solutocapillary stresses, and vapor recoil [45]

$$(\Sigma_l - \Sigma_g) \cdot \hat{\mathbf{n}} = \hat{\mathbf{n}} \kappa \sigma + \nabla_s \sigma + \sum_b j_{b,i}^2 (\rho_{l,b}^{-1} - \rho_{g,b}^{-1}) \hat{\mathbf{n}}, \tag{34}$$

where

$$\mathbf{\Sigma} = \mu \left[\nabla \mathbf{u} + (\nabla \mathbf{u})^T \right] - p \mathbb{I} \tag{35}$$

is the stress tensor, σ is the surface tension, $\kappa = \nabla \cdot \hat{\mathbf{n}}$ is the interfacial curvature, and $\nabla_s = (\mathbb{I} - \hat{\mathbf{n}}\hat{\mathbf{n}}) \cdot \nabla$ is the surface gradient. Vapor recoil (the last term on the right-hand side of (34)) is negligible under conditions of interest and can be neglected.

The surface tension of the methanol-water liquid mixture is not a simple linear combination of the surface tensions of the two pure substances. Instead, it is predicted using an empirical expression [46] based on the fits to experimental data

$$\sigma = f(Y_m)\sigma_m + [1 - f(Y_m)]\sigma_w, \tag{36}$$

where

$$f(Y_m) = Y_m \frac{1 + c_1(1 - Y_m)}{1 - c_2(1 - Y_m)}, \tag{37}$$

with empirical parameters c_1 and c_2 (see Appendix A). The surface tension of each component is assumed linear with respect to the temperature

$$\sigma_b = \sigma_b^0 + \sigma_b'(T - T_0), \tag{38}$$

where σ_b^0 is the surface tension of the pure substance at the reference temperature T_0 and $\sigma_b' = \partial \sigma_b / \partial T$ is the temperature coefficient of surface tension. With the help of (36)–(38) the term $\nabla_s \sigma$ on the right-hand-side of (34) can be rewritten as

$$\begin{aligned} \nabla_s \sigma = {} & f'(Y_m)(\sigma_m - \sigma_w) \nabla_s Y_m \\ & + \left[f(Y_m)\sigma_m' + [1 - f(Y_m)]\sigma_w' \right] \nabla_s T_i, \end{aligned} \tag{39}$$

where the first and the second term represent the soluto- and thermocapillary stresses, respectively.

Following Li and Yoda [17] we will assume that the fluid is contained in a rectangular cavity with inner dimensions $L \times W \times H$ (cf. Fig. 1) and thin walls of thickness h_s and conductivity k_s. The left end wall is cooled with a constant temperature T_c imposed on the outside, while the right end wall is heated with a constant temperature $T_h = T_c + \Delta T$ imposed on the outside. Since the walls are thin, one-dimensional conduction inside these is assumed, yielding the following mixed boundary conditions on the inside of the end walls:

$$\begin{aligned} T|_{x=0} &= T_c + k_\iota \frac{h_s}{k_s} \partial_n T, \\ T|_{x=L} &= T_h + k_\iota \frac{h_s}{k_s} \partial_n T, \end{aligned} \tag{40}$$

where $\iota = g$ ($\iota = l$) above (below) the contact line.

Since in most experiments side walls are nearly adiabatic, heat flux through the top, bottom, front, and back walls is ignored

$$\partial_n T = 0. \tag{41}$$

Standard no-slip boundary conditions $\mathbf{u} = 0$ for the velocity and no-flux boundary conditions for the concentrations

$$\begin{aligned} \partial_n X_b &= 0, \\ \partial_n Y_b &= 0 \end{aligned} \tag{42}$$

are imposed on all the walls. The pressure boundary condition follows from (2) with inertial and viscous stresses neglected:

$$\partial_n p = \rho \hat{\mathbf{n}} \cdot \mathbf{g}, \tag{43}$$

where the density ρ is a function of the local concentration and temperature.

Table 1
Types of boundary conditions imposed on various internal boundaries in the numerical implementation of the model. Periodic boundary conditions on the side walls are used in 2D, while in 3D the boundary conditions at the side walls are the same as those at the top and bottom of the cavity.

Field	Types of boundary conditions			
	Interface, gas side	Interface, liquid side	Hot/cold wall	Top/bottom wall
$\mathbf{u}$	Dirichlet	Neumann	Dirichlet	Dirichlet
p	Neumann	Dirichlet	Neumann	Neumann
T	Dirichlet	Neumann	mixed	Neumann
X_m	Neumann	–	Neumann	Neumann
X_w	Neumann	–	Neumann	Neumann
Y_m	–	Neumann	Neumann	Neumann

2.3. Implementation

The two-sided transport model described above has been implemented numerically within the open-source CFD package OpenFOAM [47], where the surface-tracking method [48] is used for describing the moving interface and the moving mesh. The details can be found in Refs. [49,50]. At the liquid-gas interface, the number fluxes due to phase change $j_{b,i}$, the interfacial temperature T_i, the saturation temperatures $T_{s,b}$, the normal component of the gas velocity $\mathbf{u}_g$ and liquid velocity $\mathbf{u}_l$, the vapor pressures p_b and $p_{s,b}$, and the normal components of the gradients of the concentration fields $\partial_n X_b$ and $\partial_n Y_w$ satisfy a set of boundary conditions, most of which are nonlinear. These interfacial fields were therefore computed simultaneously using the Newton method. The types of boundary conditions imposed at different boundaries are summarized in Table 1.

3. Results and discussion

The model described in the previous section was used to investigate the two-phase flow of a binary mixture of methanol and water under the conditions matching the experimental study of Li and Yoda [17], which used a layer of liquid of average thickness $d_l = 2.5$ mm confined in the test cell with the inner dimensions $L \times H \times W = 48.5$ mm $\times 10$ mm $\times 10$ mm (material parameters are provided in the Appendix A). For a liquid layer of this thickness, gravitational effects are substantial in terrestrial conditions. First of all, the thickness d_l is comparable to the capillary length for water, so the liquid spreads along the bottom of the cavity in a layer of reasonably uniform thickness. Since both methanol and water are volatile, the gas layer at the top of the cavity contains a mixture of methanol vapor, water vapor, and air. Furthermore, the dynamic Bond number

$$Bo_D = \frac{\beta_l \rho_l g d_l^2}{\sigma'} \tag{44}$$

ranges from 0.08 for pure water ($Y_m = 0$) to 0.41 for pure methanol ($Y_m = 1$), so that buoyancy effects could be comparable to the thermocapillary stresses [51].

While the model and its numerical implementation can describe the flows in both 2D and 3D systems, the results presented here are obtained exclusively for 2D flows (ignoring variation in the y-direction), since 3D simulations require significant computational resources and time. 2D simulations describe the central vertical (x-z) plane of the experimental test cell. Furthermore, we fixed the contact angle at 90 degrees following a previous study of this geometry [29] that showed the flow patterns in both phases to be quite insensitive to the value of the contact angle.

All simulations were initialized with the fluid being stationary and temperature being uniform, $T = T_0$ (where $T_0 = (T_c + T_h)/2 = 293$ K in all cases), the liquid layer having uniform thickness d_l and composition $Y_m = \overline{Y}_m$. The partial pressure $p_{g,b}$ of the vapors is initially set equal to the equilibrium value at $\overline{Y}_m$ and T_0, calculated using (25) and (26), and the partial pressure of air is chosen such that $X_a = \overline{X}_a$, i.e., $p_{g,a} = (p_{g,m} + p_{g,w})\overline{X}_a/(1 - \overline{X}_a)$. The temperature difference $\Delta T = T_h - T_c = 6$ K between the outer surfaces of the hot and cold end walls was set as in the experimental study, and the system was allowed to evolve until it reached an asymptotic state, either steady or time-dependent.

3.1. Dynamical regimes

The experimental study used particle image velocimetry to investigate convective patterns in the liquid layer as a function of the two concentrations, $\overline{X}_a$ and $\overline{Y}_m$. It was found that the flow pattern is most sensitive to the changes in the composition of the gas phase, which unambiguously points to the transport in the gas phase playing a key role in this problem. The dependence on the composition of the liquid phase is much weaker and was conjectured to be associated with the variation in the concentration coefficient of surface tension $|\partial\sigma/\partial Y_m|$, which controls the strength of solutocapillary stresses (cf. Fig. 4 of Ref. [17]). The results are summarized in Fig. 2, with the dashed line separating different flow regimes from each other in the $(\overline{X}_a, \overline{Y}_m)$ parameter plane. Specifically, at high $\overline{X}_a$ one finds a steady thermocapillary dominated flow (TDF), with the flow along the entire interface directed away from

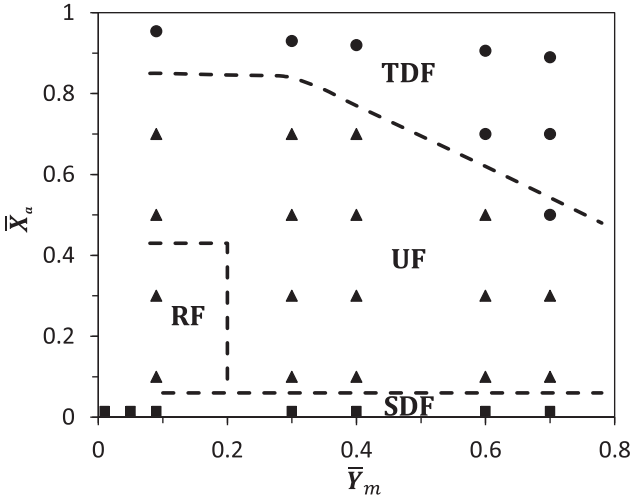

Fig. 2. The flow regimes observed at $\Delta T = 6$ K for different $\overline{Y}_m$ and $\overline{X}_a$. Dashed lines show transition boundaries between different flow regimes observed in the experiments of Li and Yoda [17] and symbols correspond to the numerical results. The three distinct flow regimes observed in the numerical simulations are: thermocapillarity dominated flow, TDF (•), unsteady flow, UF (▲), and solutocapillarity dominated flow, SDF (■). A fourth flow regime, reversed flow (RF), was only observed in the experiments.

the hot end wall (opposite the applied temperature gradient). At low $\overline{X}_a$ one finds a steady solutocapillary dominated flow (SDF), with the flow along the entire interface directed towards the hot end wall (in the direction of the applied temperature gradient). At intermediate values of $\overline{X}_a$, an unsteady flow (UF) is found with a complicated convection pattern extending over the entire thickness of the liquid layer and a substantial fraction of its horizontal extent.

At low $\overline{Y}_m$ ($\overline{Y}_m \lesssim 0.2$), the experiments identified the forth regime, reversed flow (RF). It is similar to the SDF over most of the liquid layer except very near the hot end, where the fluid at the interface moves away from the hot wall (as in TDF), forming a tiny counterclockwise recirculation zone separated from the rest of the flow. It was conjectured that, at low $\overline{Y}_m$, strong evaporation could completely remove methanol from the region inside the recirculation zone, with the liquid effectively becoming a simple fluid (pure water). This would lead to solutocapillary stresses effectively disappearing and the fluid driven away from the hot wall by a combination of thermocapillarity and buoyancy [32].

To validate our model, we performed numerical simulations over a range of methanol concentrations $\overline{Y}_m$ in the liquid and air concentrations $\overline{X}_a$ in the gas, with the results summarized as symbols in Fig. 2. A quick comparison shows that numerical results agree well with experimental observations over most of the parameter space: the same dynamical regimes are found, and the transition boundaries are overall in good agreement, even though the numerical simulations are 2D, while the flow in experiments exhibits clear 3D effects. We have not found flows consistent with RF, which could be due to the fact that the numerical simulations are 2D or that the contact angle is notably different from experiment. The big advantage of the numerical simulations is that they provide substantially more detailed information about the flow, compared with experiments. In particular, they not only resolve the fluid flow in both phases, but also describe the temperature and concentration fields in the bulk and at the interface and therefore allow a direct comparison of thermo- and solutocapillary stresses that control the flow. We describe these numerical results next.

3.2. Flow field

Since the dependence of the flow on the methanol concentration in the liquid is weak, we fix $\overline{Y}_m = 0.6$ and explore the changes in the flow associated with the variation in the air concentration $\overline{X}_a$. The flow fields at five different values of $\overline{X}_a$ are shown in Fig. 3 and the associated (time-averaged) interfacial velocity in Fig. 4. We find that the flow regimes vary from TDF at $\overline{X}_a = 0.91$ and 0.7 to UF at $\overline{X}_a = 0.5$ and 0.1 to SDF at $\overline{X}_a = 0.015$, just as in the experiment. The structure of the flow fields in the liquid layer is also found to be similar to that found in the experiment. This gradual transition from TDF to SDF associated with the decrease in $\overline{X}_a$ can be easily understood qualitatively with the help of the model described in Section 2.

At atmospheric conditions $\overline{X}_a = 0.91$, so the gas phase is dominated by air, while at the lowest concentration we considered here ($\overline{X}_a = 0.015$) the gas is dominated by the vapors. Similar studies of volatile simple fluids (e.g., 0.65 cSt silicone oil in Ref. [32]) have shown that the concentration of air (or other noncondensable gases) has a significant effect on the phase change and, as a result, the interfacial temperature distribution. Thermocapillary effects were found to be the strongest at atmospheric conditions, with phase change suppressed due to the diffusion of vapors through air. As the concentration of air is reduced, phase change is enhanced and the latent heat associated with phase change reduces the variation of the interfacial temperature along the interface. In the absence of noncondensables, the gas pressure, and hence vapor pressure and saturation temperature, all become effectively constant [30]. Since the interfacial temperature is very close to the saturation temperature [30], the interfacial temperature gradient, and hence thermocapillary stresses, also disappear.

Whether the same conclusion should necessarily apply to binary fluids is not immediately obvious. Indeed, in the absence of noncondensables, differential phase change of the two components could lead to spatial variation of the concentrations X_w and X_m, and hence the saturation temperature $T_{s,w}$ and $T_{s,m}$, of the two vapors. Although, in principle, this allows the interfacial temperature to vary spatially, it is easy to show that T_i should in fact be constant when the gas pressure p_g is constant. Since $p_{g,b} = X_b p_g$, according to (26) we can write $T_{s,b} = g_b(X_b)$, where g_m and g_w are some functions. Furthermore, since the saturation temperature of each vapor is very close to T_i, we should have $X_b = g_b^{-1}(T_i)$ and, since $X_a = 0$,

$$X_m + X_w = g_m^{-1}(T_i) + g_w^{-1}(T_i) = 1. \tag{45}$$

For generic functions g_m and g_w, this equation can only be satisfied over the entire interface for a fixed constant T_i.

In contrast, solutocapillary stresses are expected to be the weakest at atmospheric conditions when phase change that drives the variation in the liquid composition at the interface is strongly suppressed. As the concentration of air is reduced, phase change becomes stronger, with the more volatile component (methanol) accounting for the bulk of the molecules that evaporate near the hot end and condense near the cold end. This corresponds to a decrease in Y_m near the hot end and an increase in Y_m near the cold end, establishing a concentration gradient and associated solutocapillary stresses that drive the flow along the interface towards the hot end of the cavity. These stresses should be maximized when the air is removed completely and the phase change is unimpeded.

To sum up, at conditions close to atmospheric (high $\overline{X}_a$), solutocapillarity can be neglected, thermocapillary stresses dominate, and the binary fluid should behave just like a simple fluid. In particular, this explains why the stationary convection rolls observed in the liquid layer at $\overline{X}_a = 0.91$ (cf. Fig. 3(a)) almost completely disappear when $\overline{X}_a$ is decreased to 0.7 (cf. Fig. 3(b)). The linear stability analysis [51] attributes this to a decrease in the modulation of thermocapillary stresses about the (nearly constant) average associated with enhanced mass transport in the gas phase.

As the concentration of air is decreased, convection pattern reappears at around $\overline{X}_a = 0.5$, where a time-periodic pattern emerges (cf. Fig. 3(c)). It features multiple counterclockwise convection rolls in the liquid layer traveling towards the cold end of the cavity. This traveling wave is different from hydrothermal waves in simple fluids [52]: it travels in the opposite direction, as in the case of simple flows driven by a combination of thermocapillarity and buoyancy [29]. However, unlike the case of simple fluids, the instability that gives rise to this convection pattern cannot rely solely on thermocapillarity and buoyancy [51], and thus has to be due to the solutocapillary effect. Note that, away from the end walls, the time-averaged interfacial velocity, and hence thermocapillary stresses, at this $\overline{X}_a$ are nearly the same as those at $\overline{X}_a = 0.91$ (cf. Fig. 4). This is consistent with the results obtained for the interfacial temperature gradient in simple volatile fluids in the presence noncondensables [32].

Flows towards the hot wall (even locally) do not appear in the central region until $\overline{X}_a$ is reduced much further, when convection pattern becomes aperiodic in space and time. In particular, at $\overline{X}_a = 0.1$ (cf. Fig. 3(d)) we find both counterclockwise and clockwise convection rolls, with the corresponding portions of the interface featuring flow towards the cold and hot wall, respectively. It is only when almost no air remains in the system (e.g., $\overline{X}_a = 0.015$, cf.

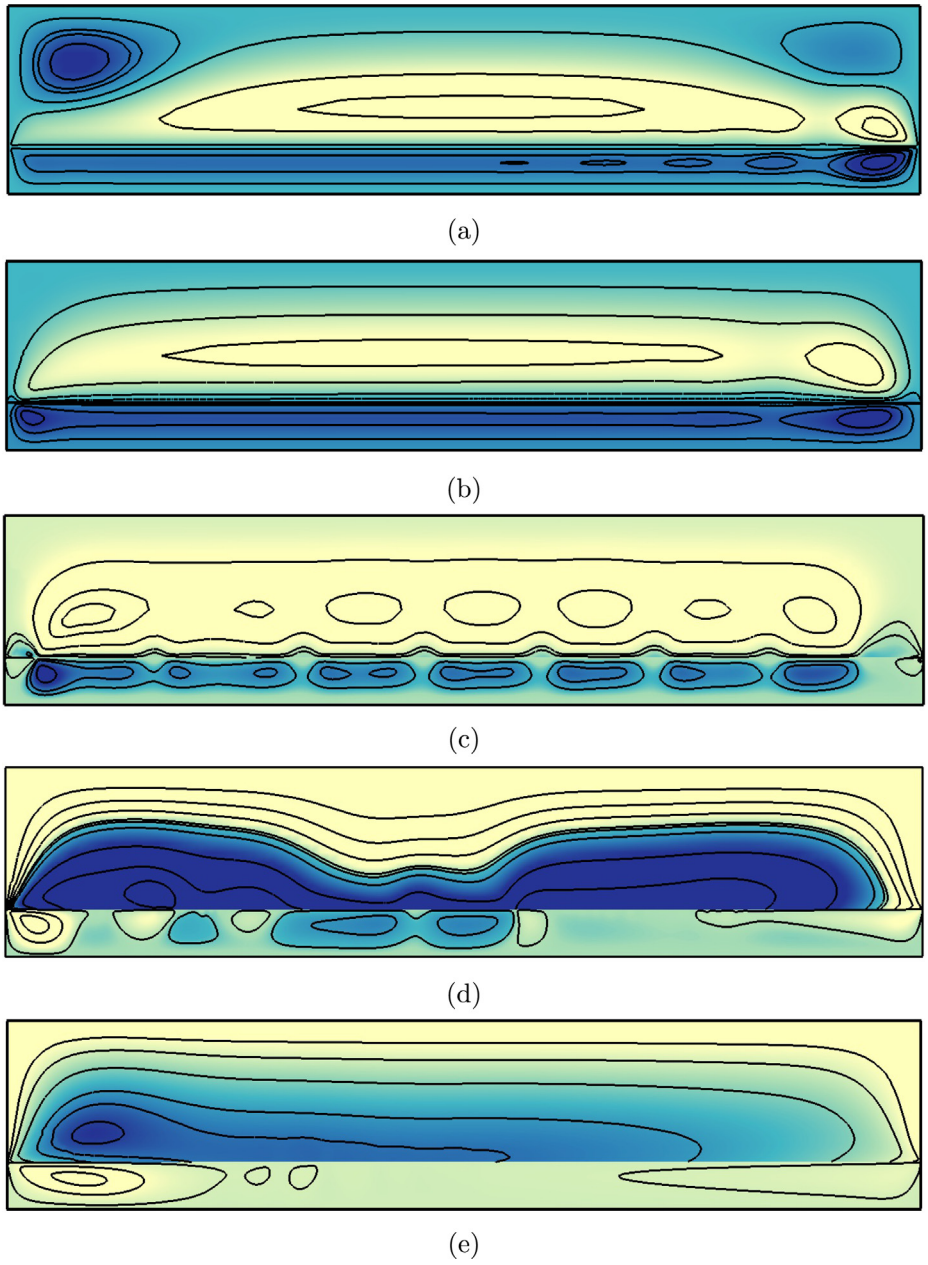

Fig. 3. Fluid flow in both phases at $\Delta T = 6$ K, $\overline{Y}_m = 0.6$ with (a) $\overline{X}_a = 0.91$, (b) $\overline{X}_a = 0.7$, (c) $\overline{X}_a = 0.5$, (d) $\overline{X}_a = 0.1$, (e) $\overline{X}_a = 0.015$. The cold end wall is on the left. Solid lines represent the streamlines of the flow. Here and below, the background represents the value of the stream function ψ, where darker (lighter) indicates higher (lower) values of ψ. High-resolution movies of the flow field are included as *supplemental material*; their duration corresponds to two periods for periodic flow at $\overline{X}_a = 0.5$, and two oscillation cycles of the convection roll next to the cold end for aperiodic flow at $\overline{X}_a = 0.1$.

Fig. 3(e)), that counterclockwise convection rolls disappear and convection pattern becomes steady again, that the flow towards the hot wall is established over the entire length of the interface. In this limit, thermocapillarity becomes negligible, and the flow is driven primarily by solutocapillary stresses (and, for sufficiently thick layers, buoyancy).

To make the comparison of solutocapillary and thermocapillary stresses more quantitative, in the next few sections we will consider the concentration and temperature fields.

3.3. Concentration field and solutocapillary stresses

Solutocapillary stresses are determined by the local composition of the liquid phase, which is strongly influenced by the advective transport. As Fig. 5 shows, the concentration field Y_m in the liquid layer reflects even the most insignificant details of the underlying flow. Unlike Y_m, the concentration field X_m in the gas layer is effectively independent of the flow pattern and remains qualitatively the same for all $\overline{X}_a$. This contrast is due to the large difference in the mass Péclet numbers

$$Pe_m = \frac{u_i d}{D}, \tag{46}$$

where d is the thickness of the layer, u_i is the characteristic magnitude of the interfacial velocity, and D is the relevant diffusion constant (D_l for the liquid, D_{mm} for the gas). Specifically, $Pe_m \sim O(10^3)$ for the liquid layer, such that mass transport is dominated by

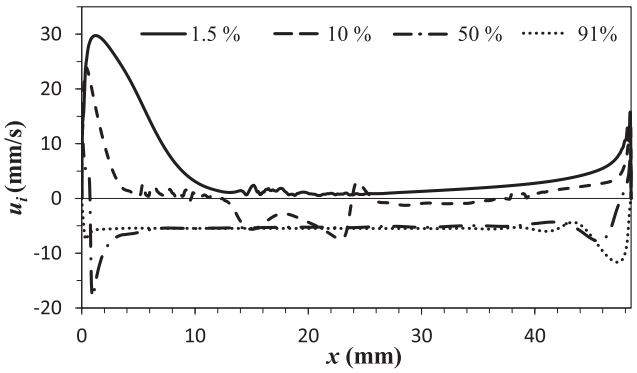

Fig. 4. Interfacial velocity at $\Delta T = 6$ K, $\overline{Y}_m = 0.6$ with different $\overline{X}_a$. For unsteady flow ($\overline{X}_a = 0.5, 0.1$), the value is averaged over a time period corresponding to the oscillation cycle of the convection roll next to the cold end.

advection, while $Pe_m \sim O(10^{-1})$ for the gas layer, such that it is diffusion that becomes the dominant transport mechanism.

Since advection controls mass transport in the liquid layer, very thin concentration boundary layers tend to form in the liquid layer just below the interface, which has two important consequences. First of all, this requires the use of meshes with high spatial resolution to properly resolve the variation in Y_m in the bulk and, consequently, along the interface. Second, while the interfacial composition, and hence solutocapillary stresses, depend sensitively on the flow in the liquid layer, they are only weakly dependent of the composition of the gas phase on the other side of the interface. As a result, when thermocapillary stresses dominate ($\overline{X}_a \gtrsim 0.5$), driving the fluid along the entire interface towards the cold end wall, advection makes the interfacial concentration Y_m essentially uniform (cf. Fig. 6), thereby effectively eliminating solutocapillary stresses

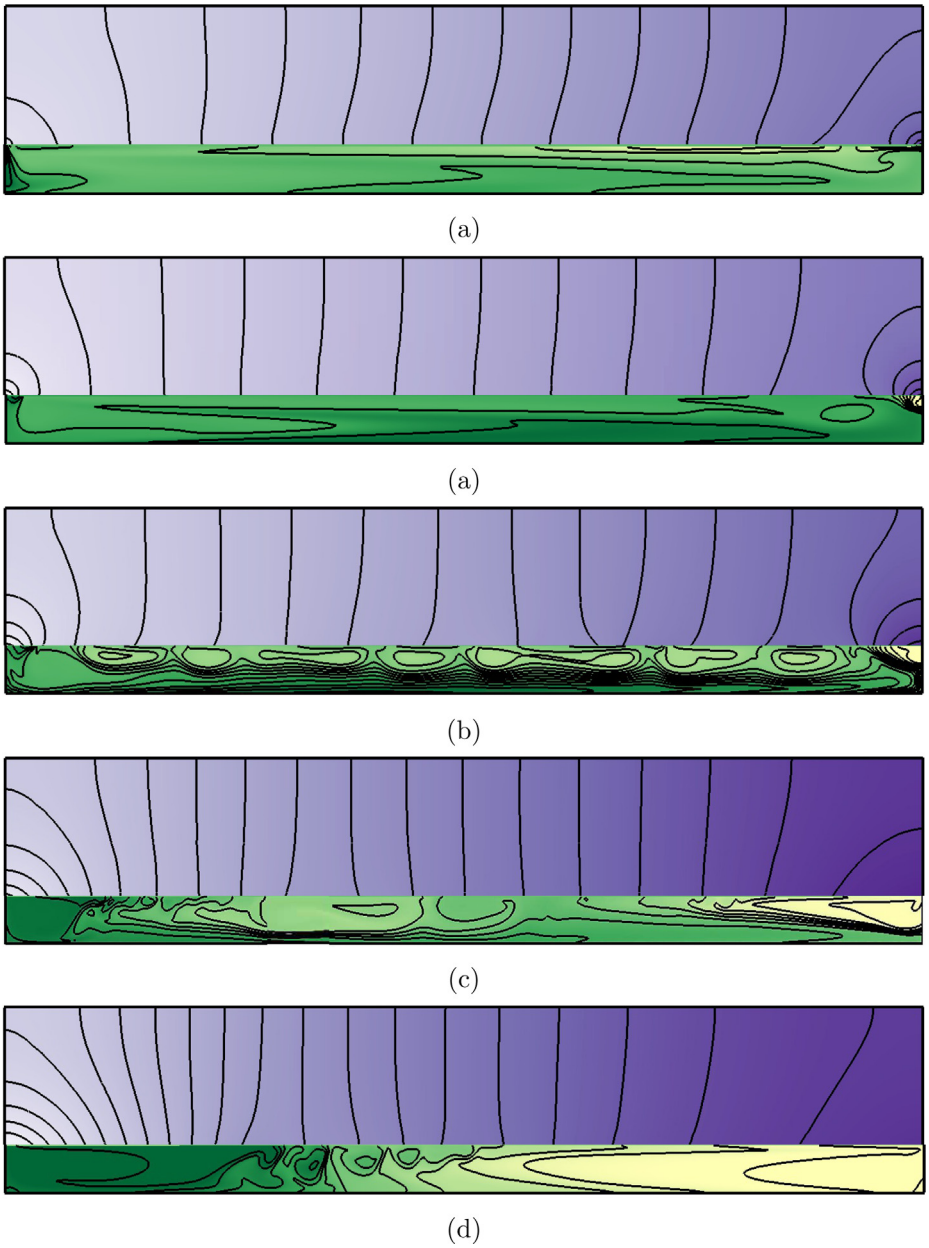

Fig. 5. Concentration of methanol in the liquid and in the gas at $\Delta T = 6$ K and $\overline{Y}_m = 0.6$ for different $\overline{X}_a$. (a) $\overline{X}_a = 0.7, Y_m = 0.6 \pm 2.88 \times 10^{-4}, X_m = 0.26 \pm 0.023$, (b) $\overline{X}_a = 0.5, Y_m = 0.6 \pm 9.31 \times 10^{-4}, X_m = 0.43 \pm 0.037$, (c) $\overline{X}_a = 0.1, Y_m = 0.6 \pm 6.95 \times 10^{-3}, X_m = 0.78 \pm 0.039$, (d) $\overline{X}_a = 0.015, Y_m = 0.6 \pm 3.35 \times 10^{-3}, X_m = 0.86 \pm 0.014$. Solid lines represent equispaced level sets of the concentration fields (15 in the liquid and 20 in the gas). In both phases, the lighter (darker) color indicates lower (higher) concentration. (For interpretation of the references to color in this figure legend, the reader is referred to the web version of this article.)

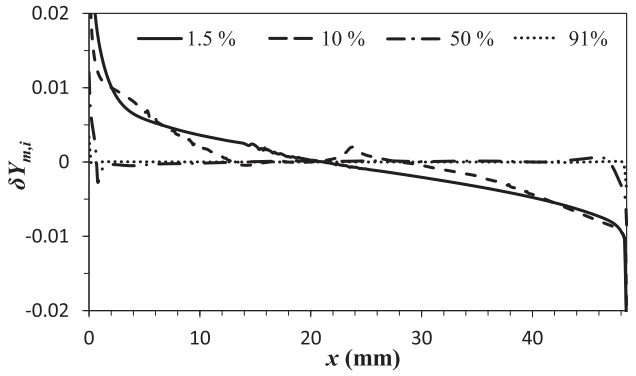

Fig. 6. Concentration of methanol (in the liquid) along the interface at $\Delta T = 6$ K, $\overline{Y}_m = 0.6$ with different $\overline{X}_a$. The vertical axis is truncated to highlight the variation $\delta Y_{m,i} = Y_{m,i} - \langle Y_{m,i} \rangle_x$ about the mean value in the central region of the cavity. For unsteady flows ($\overline{X}_a = 0.5, 0.1$), the values are averaged over a time period corresponding to the oscillation cycle of the convection roll next to the cold end.

$$\Sigma_S = f'(Y_m)(\sigma_m - \sigma_w)\partial_x Y_m, \tag{47}$$

as illustrated by Fig. 7.

Note that the magnitude of the derivative $f'(Y_m)$ in (47) increases as Y_m decreases, according to (37), leading to an increase in the solutocapillary stresses at the same concentration gradient $\partial_x Y_m$. This is the origin of the weak dependence on $\overline{Y}_m$ in the regime diagram shown in Fig. 2.

For $\overline{Y}_m = 0.6$, a significant concentration gradient $\partial_x Y_m$ only appears when $\overline{X}_a$ is decreased to around 0.1, at which point the adverse effect of air on phase change is reduced substantially and the differential phase change becomes strong enough to compete with the advective transport in the liquid. At this value of $\overline{X}_a$, the flow is unsteady and features convection rolls rotating in opposite directions, which causes the interfacial concentration gradient to be nonmonotonic and even change sign (cf. Fig. 6), which is reflected in the spatial profile of the solutocapillary stresses (cf. Fig. 7). Note that the concentration gradient is first established near the end walls, where phase change is the most intense. A concentration gradient of the same sign is established across the entire interface only at very low $\overline{X}_a$ (e.g., $\overline{X}_a = 0.015$), when, on the one hand, phase change is essentially unimpeded by the presence of air and, on the other hand, thermocapillary stresses become sufficiently weak. In this limit, solutocapillary stresses exceed thermocapillary stresses, driving the fluid along the entire interface towards the hot end wall, with advection in the liquid layer smoothing out the interfacial concentration gradients (cf. Fig. 6).

While the concentration fields in the liquid layer are very complicated, the concentration fields in the gas layer are quite simple and very smooth, since mass transport there is controlled by diffusion and is therefore essentially independent of the flow field. As Fig. 5 shows, away from the end walls, the gradient of methanol concentration X_m in the vertical direction is negligible compared with the gradient in the horizontal direction, suggesting that mass transport in gas phase is effectively one-dimensional. A similar conclusion has been made for two-phase flow of a simple fluid [32], which allowed a simplified transport model to explain the observed concentration profiles and interfacial temperature profiles, which are both exponential in x. As Fig. 8 illustrates, the concentration profile in the ternary gas mixture in the present problem is also exponential in the central portion of the cavity, with the characteristic length scale that increases with $\overline{X}_a$. At high $\overline{X}_a$, when phase change is suppressed, the characteristic length becomes larger than the length L of the cavity, and the concentration profile becomes essentially linear.

3.4. Temperature field and thermocapillary stresses

Just like the concentration fields, the temperature fields in the two layers (shown in Fig. 9) have a distinctly different character. Once again, we find that the temperature field in the liquid layer has a lot of fine structure reflecting the details of the underlying flow, while the temperature field in the gas layer is effectively independent of the flow and remains qualitatively the same over the entire range of $\overline{X}_a$, with the difference due almost entirely to the boundary condition at the interface (cf. Fig. 10). Hence we can arrive at a similar conclusion that heat transport in the gas phase is controlled by diffusion, while heat transport in the liquid phase is controlled by advection. Indeed, the thermal Péclet number(See Fig. 11)

$$Pe_t = \frac{u_i d}{\alpha}, \tag{48}$$

is $O(1)$ for the gas layer and $O(10^2)$ for the liquid layer, reflecting the large difference in the thermal diffusivities of the two layers.

In contrast with the concentration field, it is the interfacial temperature T_i that controls the bulk temperature field in both layers, as Fig. 9 illustrates. Indeed, as Fig. 10 shows, T_i is a very smooth and monotonic function of position (aside from some minor modulation), even when an unsteady convection flow is found in the liquid layer. This is due to a large amount of latent heat absorbed

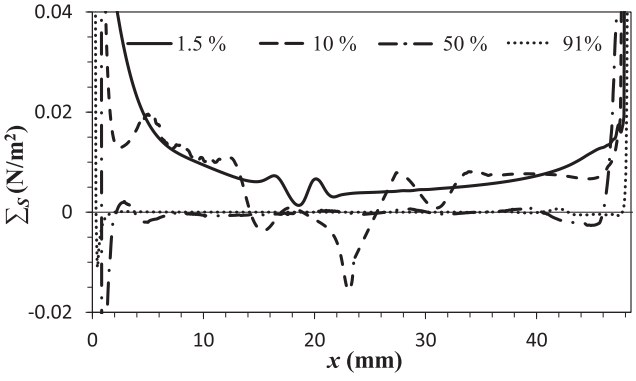

Fig. 7. Solutocapillary stresses Σ_S at $\Delta T = 6$ K, $\overline{Y}_m = 0.6$ with different $\overline{X}_a$. The vertical axis is truncated to highlight the variation of Σ_S in the central region of the cavity. For unsteady flow ($\overline{X}_a = 0.5, 0.1$), the value is averaged over a time period corresponding to the oscillation cycle of the convection roll next to the cold end.

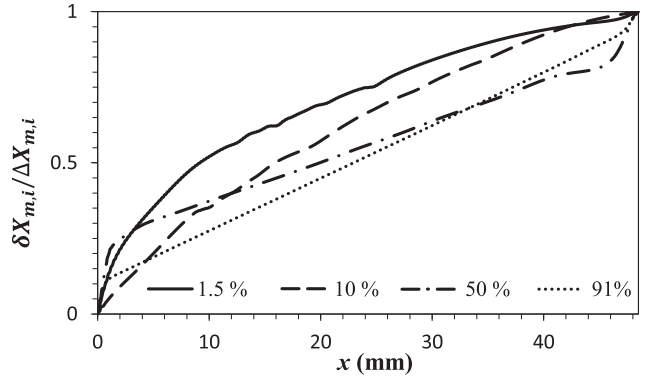

Fig. 8. Concentration of methanol (vapor) along the interface at $\Delta T = 6$ K, $\overline{Y}_m = 0.6$ with different $\overline{X}_a$. Deviation $\delta X_{m,i} = X_{m,i}|_x - X_{m,i}|_{x=0}$ from the mean is normalized by the total variation $\Delta X_{m,i}$ along the interface. For unsteady flow ($\overline{X}_a = 0.5, 0.1$), the value is averaged over a time period corresponding to the oscillation cycle of the convection roll next to the cold end.

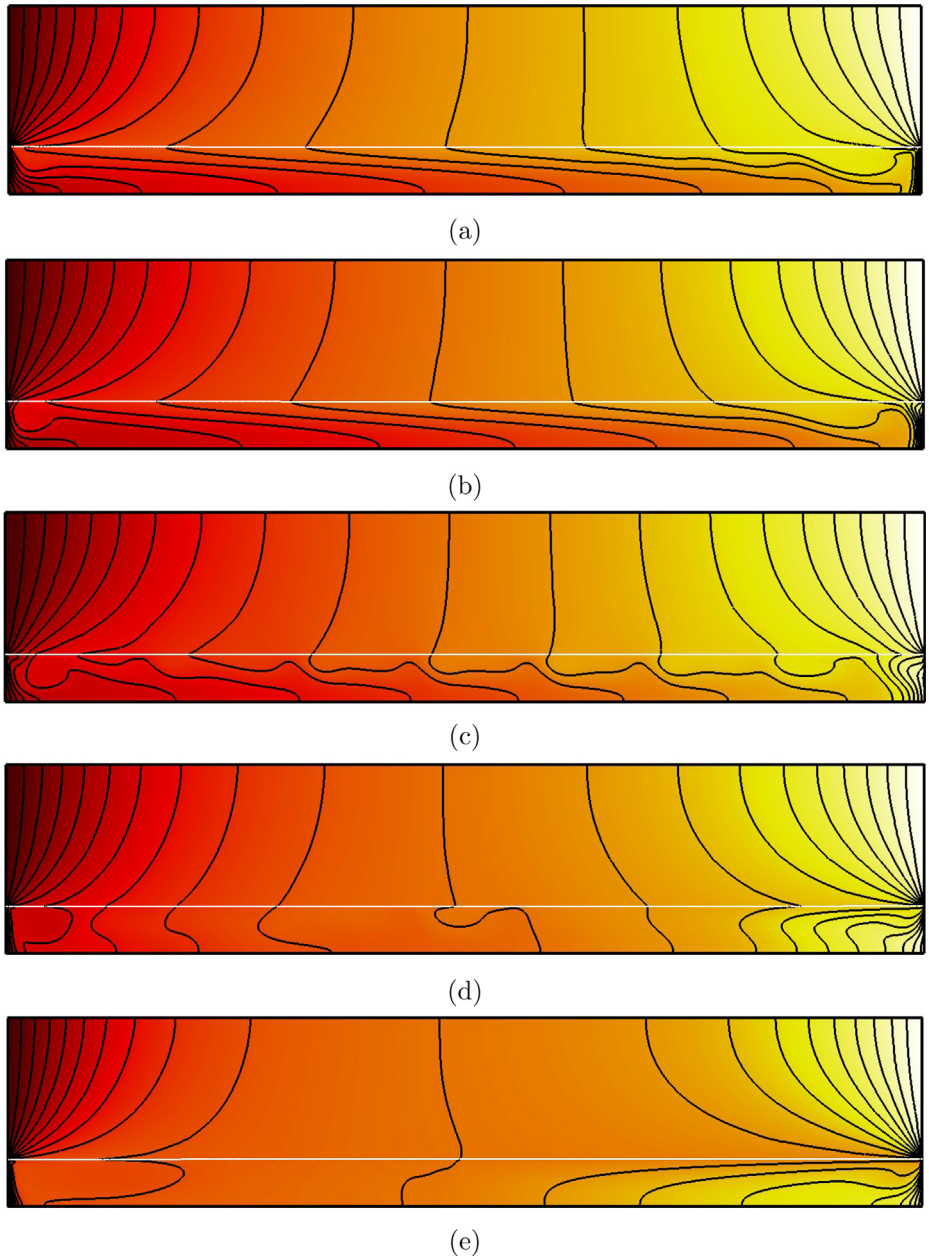

Fig. 9. The temperature field T in both phases at $\Delta T = 6$ K, $\overline{Y}_m = 0.6$, and (a) $\overline{X}_a = 0.91$, (b) $\overline{X}_a = 0.7$, (c) $\overline{X}_a = 0.5$, (d) $\overline{X}_a = 0.1$, (e) $\overline{X}_a = 0.015$. The lighter (darker) color corresponds to higher (lower) temperature. Solid lines represent the twenty equally spaced isotherms and the horizontal white solid line denotes the liquid-gas interface. (For interpretation of the references to colour in this figure legend, the reader is referred to the web version of this article.)

or released at the interface during phase change, which results in the interfacial temperature being determined by the composition of the gas layer, $T_i = g_m(X_m)$, where X_m varies smoothly and monotonically in the horizontal direction, as discussed in the previous section. Note that, in the central region, the interfacial temperature has an exponential profile mirroring the methanol concentration in the gas phase (cf. Fig. 8).

Since X_m and Y_m vary relatively little about their spatial mean, thermocapillary stresses Σ_T

$$\begin{aligned}\Sigma_T &= [f(Y_m)\sigma'_m + [1 - f(Y_m)]\sigma'_w]\partial_x T_i \\ &\approx [f(\overline{Y}_m)\sigma'_m + [1 - f(\overline{Y}_m)]\sigma'_w]g'_m(\overline{X}_m)\partial_x X_m \end{aligned} \quad (49)$$

are essentially controlled by the interfacial concentration gradient $\partial_x X_m$ in the gas phase. As this concentration gradient decreases with decreasing $\overline{X}_a$, so does the interfacial temperature gradient and the thermocapillary stresses, until both essentially disappear at $\overline{X}_a = 0$.

To sum up, a quantitative analysis of the concentration and temperature fields shows that solutocapillary and thermocapillary stresses are controlled by the concentration fields in the liquid and gas layer, respectively. Thermocapillary stresses dominate at high $\overline{X}_a$ and solutocapillary stresses dominate at low $\overline{X}_a$, as predicted from qualitative considerations in Section 3.1. Since the flow at intermediate values of $\overline{X}_a$ is unsteady, no sharp transition from TDF to SDF is observed at $\Delta T = 6$ K. Unsteady flow should disappear at lower ΔT, enabling a more direct comparison between the experimental or numerical results and analytical predictions.

4. Summary and conclusions

We have introduced, implemented, and validated a comprehensive transport model for two-phase flows of volatile binary fluids in confined geometries. The model accounts for momentum, mass,

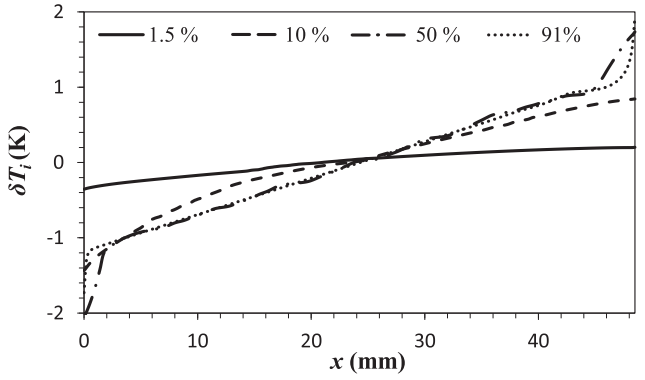

Fig. 10. Interfacial temperature T_i at $\Delta T = 6$ K, $\overline{Y}_m = 0.6$ with different $\overline{X}_a$. The vertical axis is truncated to highlight the variation $\delta T_i = T_i - \langle T_i \rangle_x$ about the mean in the central region of the cavity. For unsteady flow ($\overline{X}_a = 0.5, 0.1$), the values are averaged over a time period corresponding to the oscillation cycle of the convection roll next to the cold end.

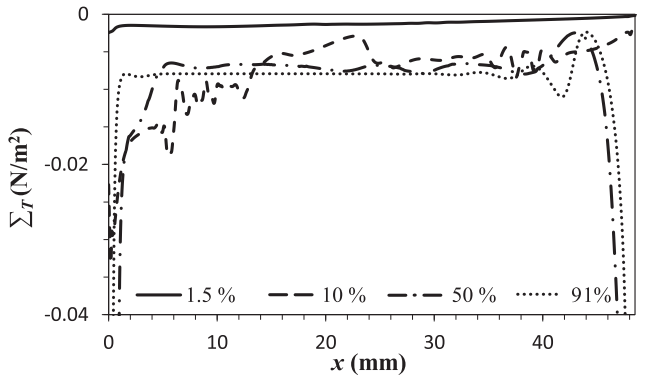

Fig. 11. Thermocapillary stresses Σ_T at $\Delta T = 6$ K, $\overline{Y}_m = 0.6$ with different $\overline{X}_a$. The vertical axis is truncated to highlight the variation of Σ_T in the central region of the cavity. For unsteady flow ($\overline{X}_a = 0.5, 0.1$), the values are averaged over a time period corresponding to the oscillation cycle of the convection roll next to the cold end.

and heat transport in both phases, as well as phase change at the liquid-gas interface. It should be emphasized that, with straightforward modifications, the model can also describe transport in mixtures of an arbitrary number of miscible components with arbitrary composition. The numerical model was used to investigate buoyancy-Marangoni convection in water-methanol mixture confined inside a sealed rectangular cavity, which arises when a horizontal temperature gradient is imposed. Although the numerical simulations were confined to two spatial dimensions, their results are found to be in good agreement with experimental observations [17].

The presence of air inside the cavity was found to have a significant effect on the flow in both phases. When the concentration $\overline{X}_a$ of air in the gas phase is high, differential phase change is greatly suppressed, solutocapillary stresses are negligible, and thermocapillarity stresses dominate. In this limit, the binary mixture behaves like a simple fluid, with a combination of thermocapillary stresses and buoyancy driving the flow away from the hot end along the entire interface. At low $\overline{X}_a$, thermocapillary stresses are suppressed and solutocapillary stresses are enhanced. As a result, the direction of the flow along the entire interface is reversed, with the fluid flowing towards, rather than away from, the hot end. Buoyancy is too weak in this problem to have much of an effect on the direction of the mean flow, although is likely plays an important role in its stability.

Interestingly, both thermocapillary stresses and solutocapillary stresses are found to be controlled by the mass transport. In particular, the thermocapillary stresses are controlled by the concentration of the two vapors in the gas phase (X_w and X_m). At high $\overline{X}_a$, the effective diffusion coefficients $\mathbb{D}_{mm}$ and $\mathbb{D}_{ww}$ are low, which leads to a large gradient of the vapor concentrations and, consequently, a large gradient in the interfacial temperature and large thermocapillary stresses. As $\overline{X}_a$ decreases, so do the vapor concentration gradients, the interfacial temperature gradient, and the thermocapillary stresses, until they all essentially disappear as $\overline{X}_a \to 0$.

The solutocapillary stresses, in turn, are controlled by the concentration of the two components of the liquid phase (Y_w and Y_m). At high $\overline{X}_a$, advection in the liquid layer is strong and the differential phase change is weak, which results in an effectively uniform composition of the liquid at interface, making solutocapillary stresses negligible. As $\overline{X}_a$ decreases, the differential phase change becomes stronger, leading to an increase in the interfacial concentration gradient and the associated solutocapillary stresses. The interfacial concentration gradient, and hence the solutocapillary stresses, become the largest as $\overline{X}_a \to 0$, when noncondensables do not impede phase change.

As Fig. 2 shows, the boundaries between different flow regimes are shifted towards smaller values of $\overline{X}_a$, highlighting the asymmetry between thermocapillary and solutocapillary stresses. There are two reasons for this. Although the temperature and concentration are described by similar transport equations, the mass diffusion coefficient D_l is much lower than the corresponding heat diffusion coefficient α_l, so that advection in the liquid layer plays a more important role in suppressing the interfacial concentration gradient compared with the interfacial temperature gradient. Furthermore, phase change leads to a large amount of heat released/absorbed at the interface, which has a correspondingly large effect on the temperature field. The effect of phase change on the interfacial composition of the liquid is much weaker, since the density of the vapors is much lower than the density of the liquid.

Despite its apparent complexity, the transport model can be simplified dramatically by focusing on mass transport in the gas phase. For cavities with reasonably high aspect ratios L/H, this should allow one to obtain approximate analytical solutions for the steady state interfacial temperature and concentration profiles (and hence thermo- and solutocapillary stresses), that can be used to predict when the transition between thermocapillary- and solutocapillary-dominated flows occurs as $\overline{X}_a$ varies. Such analysis has already been performed and discussed in a subsequent publication Ref. [53].

Conflict of interest

Authors declared that there is no conflict of interest.

Acknowledgments

This work was supported by the National Science Foundation under Grant No. CMMI-1511470.

Appendix A. Material properties

The walls of the test cell are made of quartz (fused silica) with thermal conductivity $k_s = 1.4$ W/m-K and have a thickness $h_s = 1.25$ mm.

The material properties of methanol, water, and air are summarized in Table A.1. The binary diffusion coefficients are $D_l = 1.29 \times 10^{-9}$ m^2/s, $D_{mw} = 1.65 \times 10^{-5}$ m^2/s, $D_{ma} = 1.50 \times 10^{-5}$ m^2/s, and $D_{wa} = 2.50 \times 10^{-5}$ m^2/s. The activity coefficients γ are calculated based on the UNIFAC (UNIQUAC Functional-group

Table A.1
Material properties of pure components at the reference temperature $T_0 = 293$ K (cf. Refs. [55,56]). The maximum reported value for enthalpy of mixing between the water and methanol is −0.96 kJ/mol [57], when the concentration of methanol is around 0.31.

	Methanol		Water		Air
	Liquid	Vapor	Liquid	Vapor	
μ (kg/(m·s))	5.78×10^{-4}	9.44×10^{-6}	9.94×10^{-4}	9.80×10^{-6}	1.81×10^{-5}
ρ (kg/m^3)	792	0.167	998	0.017	1.20
β (1/K)	1.13×10^{-3}	3.41×10^{-3}	2.07×10^{-4}	3.41×10^{-3}	3.41×10^{-3}
k(W/(m·K))	0.203	0.013	0.597	0.018	0.026
C_p (J/kg)	2.57×10^3	1.36×10^3	4.23×10^3	1.86×10^3	1.00×10^3
σ (N/m)	2.42×10^{-2}		7.23×10^{-2}		-
σ' (N/(m·K))	-1.35×10^{-4}		-1.50×10^{-4}		-
$\mathcal{L}$ (J/mol)	3.51×10^4		4.06×10^4		-

Activity Coefficients) method [54]. For the binary water-methanol mixture at $Y_m = 0.6, \gamma_m = 1.088, \gamma_w = 1.355$.

The Antoine coefficients are $A = 23.52, B = 3645, C = -34.05$ for methanol and $A = 23.44, B = 3969, C = -40.07$ for water. The empirical parameters in the expression (36) are $c_1 = 0$ and $c_2 = 0.87$.

Appendix B. Supplementary material

Supplementary data associated with this article can be found, in the online version, at https://doi.org/10.1016/j.ijheatmasstransfer.2018.06.141.

References

[1] J. Zhang, R.P. Behringer, A. Oron, Marangoni convection in binary mixtures, Phys. Rev. E 76 (1) (2007) 016306.
[2] J. Zhang, A. Oron, R.P. Behringer, Novel pattern forming states for Marangoni convection in volatile binary liquids, Phys. Fluids 23 (7) (2011) 072102.
[3] K.E. Uguz, R. Narayanan, Instability in evaporative binary mixtures. I. The effect of solutal Marangoni convection, Phys. Fluids 24 (2012) 094101.
[4] K.E. Uguz, R. Narayanan, Instability in evaporative binary mixtures. II. The effect of Rayleigh convection, Phys. Fluids 24 (2012) 094102.
[5] H. Machrafi, A. Rednikov, P. Colinet, P.C. Dauby, Time-dependent Marangoni-Bénard instability of an evaporating binary-liquid layer including gas transients, Phys. Fluids 25 (8) (2013) 084106.
[6] E.M. Sparrow, E. Marschall, Binary, gravity-flow film condensation, J. Heat Transf. 91 (1968) 205–211.
[7] A. Tamir, Y. Taitel, E. Schlünder, Direct contact condensation of binary mixtures, Int. J. Heat Mass Transf. 17 (10) (1974) 1253–1260.
[8] R. Taylor, R. Krishnamurthy, J.S. Furno, R. Krishna, Condensation of vapor mixtures. 1. Nonequilibrium models and design procedures, Indus. Eng. Chem. Process Des. Dev. 25 (1) (1986) 83–97.
[9] K. Hijikata, Y. Fukasaku, O. Nakabeppu, Theoretical and experimental studies on the pseudo-dropwise condensation of a binary vapor mixture, J. Heat Transf. 118 (1996) 140–147.
[10] K. Kanatani, Stability of a condensing liquid film in a binary vapor mixture system, Int. J. Heat Mass Transf. 58 (1) (2013) 413–419.
[11] Y. Abe, About self-rewetting fluids-possibility as a new working fluid, Therm. Sci. Eng. 12 (3) (2004) 9–18.
[12] P. Neogi, Tears-of-wine and related phenomena, J. Colloid Interface Sci. 105 (1) (1985) 94–101.
[13] J. Fournier, A. Cazabat, Tears of wine, EPL (Europhys. Lett.) 20 (6) (1992) 517.
[14] D.C. Venerus, D.N. Simavilla, Tears of wine: new insights on an old phenomenon, Sci. Rep. 5 (2015) 16162.
[15] N. di Francescantonio, R. Savino, Y. Abe, New alcohol solutions for heat pipes: Marangoni effect and heat transfer enhancement, Int. J. Heat Mass Transf. 51 (2008) 6199–6207.
[16] A. Cecere, R. Paola, R. Savino, Y. Abe, L. Carotenuto3, S. Vaerenbergh, Observation of Marangoni flow in ordinary and self-rewetting fluids using optical diagnostic systems, Eur. Phys. J. Special Top. 192 (2011) 109–120.
[17] Y. Li, M. Yoda, An experimental study of buoyancy-Marangoni convection in confined and volatile binary fluids, Int. J. Heat Mass Trans. 102 (2016) 369–380.
[18] T.T. Nguyen, A. Kundan, P.C. Wayner Jr., J.L. Plawsky, D.F. Chao, R.J. Sicker, The effect of an ideal fluid mixture on the evaporator performance of a heat pipe in microgravity, Int. J. Heat Mass Transf. 95 (2016) 765–772.
[19] P. Kolodner, C. Surko, H. Williams, Dynamics of traveling waves near the onset of convection in binary fluid mixtures, Physica D 37 (1-3) (1989) 319–333.
[20] A. Bergeon, D. Henry, H. Benhadid, L. Tuckerman, Marangoni convection in binary mixtures with Soret effect, J. Fluid Mech. 375 (1998) 143–177.
[21] A. Bergeon, E. Knobloch, Oscillatory Marangoni convection in binary mixtures in square and nearly square containers, Phys. Fluids 16 (2) (2004) 360–372.
[22] A. Podolny, A. Nepomnyashchy, A. Oron, Long-wave coupled Marangoni-Rayleigh instability in a binary liquid layer in the presence of the Soret effect, Math. Modell. Nat. Phenomena 3 (1) (2008) 1–26.
[23] J. Platten, P. Costesèque, Charles Soret, A short biographya, Eur. Phys. J. E 15 (2004) 235–239.
[24] J. Kern, P. Stephan, Theoretical model for nucleate boiling heat and mass transfer of binary mixtures, J. Heat Transfer-Trans. ASME 125 (2003) 1106–1115.
[25] S. Karpitschka, F. Liebig, H. Riegler, Marangoni contraction of evaporating sessile droplets of binary mixtures, Langmuir 33 (2017) 4682–4687.
[26] S. Zhou, L. Zhou, X. Du, Y. Yang, Heat transfer characteristics of evaporating thin liquid film in closed microcavity for self-rewetting binary fluid, Int. J. Heat Mass Transf. 108 (2017) 136–145.
[27] T. Qin, R.O. Grigoriev, Convection, evaporation, and condensation of simple and binary fluids in confined geometries, in: Proc. of the 3rd Micro/Nanoscale Heat & Mass Transfer International Conference, MNHMT2012–75266, 2012.
[28] J.-J. Yu, Y.-R. Li, C.-M. Wu, J.-C. Chen, Three-dimensional thermocapillary-buoyancy flow of a binary mixture with Soret effect in a shallow annular pool, Int. J. Heat Mass Transf. 90 (2015) 1071–1081.
[29] T. Qin, Ž. Tuković, R.O. Grigoriev, Buoyancy-thermocapillary convection of volatile fluids under atmospheric conditions, Int. J Heat Mass Transf. 75 (2014) 284–301.
[30] T. Qin, Ž. Tuković, R.O. Grigoriev, Buoyancy-thermocapillary Convection of Volatile Fluids under their vapors, Int. J Heat Mass Transf. 80 (2015) 38–49.
[31] T. Qin, R.O. Grigoriev, The effect of noncondensables on buoyancy-thermocapillary convection in confined and volatile fluids, in: Proc. of 11th AIAA/ASME Joint Thermophysics and Heat Transfer Conference, AIAA Aviation and Aeronautics Forum and Exposition, AIAA2014–1898558, 2014.
[32] T. Qin, R.O. Grigoriev, The effect of noncondensables on buoyancy-thermocapillary convection of volatile fluids in confined geometries, Int. J Heat Mass Transf. 90 (2015) 678–688.
[33] R. Krishna, J. Wesselingh, The Maxwell-Stefan approach to mass transfer, Chem. Eng. Sci. 52 (6) (1997) 861–911.
[34] R. Taylor, R. Krishna, Multicomponent Mass Transfer, vol. 2, John Wiley & Sons, 1993.
[35] H. Toor, Solution of the linearized equations of multicomponent mass transfer: I, AIChE J. 10 (4) (1964) 448–455.
[36] H. Toor, Solution of the linearized equations of multicomponent mass transfer: II. Matrix methods, AIChE J. 10 (4) (1964) 460–465.
[37] W.E. Stewart, R. Prober, Matrix calculation of multicomponent mass transfer in isothermal systems, Indus. Eng. Chem. Fundam. 3 (3) (1964) 224–235.
[38] D.F. Fairbanks, C.R. Wilke, Diffusion coefficients in multicomponent gas mixtures, Indus. Eng. Chem. 42 (3) (1950) 471–475.
[39] R.B. Bird, W.E. Stewart, E.N. Lightfoot, Transport Phenomena, Wiley, New York, 1960.
[40] H. Kubota, Y. Yamanaka, I. Dalla Lana, Effective diffusivity of multi-component gaseous reaction system, J. Chem. Eng. Jpn. 2 (1) (1969) 71–75.
[41] A. Burghardt, R. Krupiczka, Convective mass transfer in multicomponent systems analysis and relationship defining mass transfer coefficients, Inzynieria Chem 5 (1975) 487–510.
[42] S. Kato, H. Inazumi, S. Suzuki, Mass transfer in a ternary gaseous phase, Int. Chem. Eng. 21 (1981) 443–452.
[43] J.L. Plawsky, M. Ojha, A. Chatterjee, P.C. Wayner Jr., Review of the effects of surface topography, surface chemistry, and fluid physics on evaporation at the contact line, Chem. Eng. Commun. 196 (5) (2008) 658–696.
[44] R.W. Schrage, A Theoretical Study of Interface Mass Transfer, Columbia University Press, New York, 1953.
[45] A. Oron, S.H. Davis, S.G. Bankoff, Long-scale evolution of thin liquid films, Rev. Mod. Phys. 69 (3) (1997) 931–980.
[46] G. Vazquez, E. Alvarez, J.M. Navaza, Surface tension of alcohol water+ water from 20 to 50. degree. C, J. Chem. Eng. Data 40 (1995) 611–614.
[47] <http://www.openfoam.com>.
[48] Ž. Tuković, H. Jasak, A moving mesh finite volume interface tracking method for surface tension dominated interfacial fluid flow, Comput. Fluids 55 (2012) 70–84.

[49] T. Qin, Buoyancy-Thermocapillary Convection of Volatile Fluids in Confined and Sealed Geometries (Ph.D. thesis), Georgia Institute of Technology, 2016.
[50] T. Qin, Buoyancy-Thermocapillary Convection of Volatile Fluids in Confined and Sealed Geometries (Springer Theses), Springer International Publishing, ISBN 9783319613314, 2017.
[51] R.O. Grigoriev, T. Qin, The effect of phase change on stability of convective flow in a layer of volatile liquid driven by a horizontal temperature gradient, J. Fluid Mech. 838 (2018) 248–283.
[52] M.K. Smith, S.H. Davis, Instabilities of dynamic thermocapillary liquid layers. Part 1. Convective instabilities, J. Fluid Mech. 132 (1983) 119–144.
[53] T. Qin, R.O. Grigoriev, The effect of gas-phase transport on buoyancy-Marangoni convection in confined volatile binary fluids, Phys. Rev. Fluids Under Review.
[54] A. Fredenslund, R.L. Jones, J.M. Prausnitz, Group-contribution estimation of activity coefficients in nonideal liquid mixtures, AIChE J. 21 (6) (1975) 1086–1099.
[55] C.L. Yaws, Yaws' Handbook of Thermodynamic and Physical Properties of Chemical Compounds (Electronic Edition): physical, thermodynamic and transport properties for 5,000 organic chemical compounds, Knovel, Norwich, 2003.
[56] C.L. Yaws, Yaws' Thermophysical Properties of Chemicals and Hydrocarbons (Electronic Edition), Knovel, Norwich, 2009.
[57] Methanol-Water Enthalpy of Mixing: Datasheet from Dortmund Data Bank (DDB) - Thermophysical Properties Edition 2014 in Springer Materials, 2014.